

Magnetotransport and Berry phase Tuning in Gd-doped Bi₂Se₃ Topological Insulator Single Crystals

Lei Chen¹, Shuang-Shuang Li², Weiyao Zhao^{3,4}, Abdulhakim Bake^{4,5}, David Cortie^{4,5}, Xiaolin Wang^{4,5}, Julie Karel³, Han Li^{†,1}, and Ren-Kui Zheng^{1,*}

¹School of Physics and Materials Science, Guangzhou University, Guangzhou 510006, China

²School of Materials Science and Engineering and Jiangxi Engineering Laboratory for Advanced Functional Thin Films, Nanchang University, Nanchang 330031, P. R. China

³Department of Materials Science & Engineering, and ARC Centre of Excellence in Future Low-Energy Electronics Technologies, Monash University, Clayton VIC 3800, Australia

⁴ISEM, University of Wollongong, North Wollongong NSW 2500, Australia

⁵ARC Centre of Excellence in Future Low-Energy Electronics Technologies, University of Wollongong, North Wollongong NSW 2500, Australia

The Berry phase is an important concept in solids, correlated to the band topology, axion electrodynamics and potential applications of topological materials. Here, we investigate the magnetotransport and Berry phase of rare earth element Gd doped Bi₂Se₃ (Gd:Bi₂Se₃) topological insulator at low temperatures and high magnetic fields. Gd:Bi₂Se₃ single crystals show Shubnikov-de Haas (SdH) oscillations with nontrivial Berry phase while Bi₂Se₃ single crystals show zero Berry phase in SdH oscillations. The temperature dependent magnetization curves can be well fitted with the Curie-Weiss law in 3–300 K region, indicating no magnetic ordering in Gd:Bi₂Se₃ crystals. Moreover, Gd doping has limited influence on the quantum oscillation parameters (e.g., frequency of oscillations, the area of the Fermi surface, effective electron mass, Fermi wave vectors etc.), but has an impact on the Hall mobility, carrier density,

E-mail: *zrk@ustc.edu; †lihan@gzhu.edu.cn

and band topology. Our results demonstrate that Gd doping can tune the Berry phase of topological insulators effectively, which may pave a way for the future realization of many predicted exotic transport phenomena of topological origin.

I. Introduction

The Berry phase, an important concept in many fields of physics, was proposed by Berry in 1984 [1]. The Berry phase is a Hamiltonian in a parameter space that can acquire a geometrical phase after undergoing a closed trajectory in adiabatic changes. This geometrical phase is only determined by the properties related to closed trajectory in a parameter space. In a crystal, Zak [2] argued that the Berry phase can be obtained on a moving electron in the Brillouin zone (as parameter space). As a result, the Berry phase of electrons of metals appears in the semiclassical quantization condition for its energy levels (Landau levels), which thus affects the Landau-level-related physical phenomena, e.g., Shubnikov-de Haas oscillations and de Haas-van Alphen oscillations [3,4]. The non-zero Berry phase correction to Landau quantization happens on electron orbits that link to band-contact lines, which demonstrates the Bloch band topology in solids [3]. The non-zero (nontrivial) Berry phase has been reported in Dirac semimetals [5-8], Weyl semimetals [9-11], topological nodal-line semimetals [12-18], and other topological materials [19-22]. Since the Berry phase is related to the band topology, the experimental observation is different in various materials: e.g., $\sim 0.75\pi$ and π in graphite and graphene [23,24], π in Rashba semiconductor BiTeI [25], $0.25-0.75\pi$ in Cd_3As_2 [7,8].

The quantum oscillation behaviors are normally observed in metallic materials. However, recent reports broaden this knowledge in various insulating materials with special bulk-band symmetries and metallic surface states, e.g., SmB_6 [26,27], YbB_{12} [28], Te [29], (V,

Sn):Bi_{1.1}Sb_{0.9}Te₂S [30]. The most discussed materials family is the three-dimensional (3D) topological insulators (TIs), which possess insulating bulk band and time-reversal-symmetry-protected Dirac surface state which was theoretically predicted in Bi₂Se₃ family [31] and experimental verified [32] in the last decade. The symmetry-protected surface state offers tremendous opportunities for spintronics, non-Abelian quantum computing, and energy-efficient electronic devices. Due to the Dirac band nature of the 3D TI's surface state, one may obtain the π Berry phase shift on their Landau quantization related phenomena. However, in practice, the Berry phase situation for a 3D TI can be very complicated, for example, defects shift bulk Fermi level into conduction band in Bi₂Se₃ single crystals, resulting in non-Dirac bulk-dominant quantum oscillations with zero Berry phase [33]. Even for surface dominant transport of 3D TIs, the deviation of the surface state's dispersion from ideal linearity results in nontrivial Berry phase between zero and π , e.g., 0.44π in Bi₂Te₂Se [34,35].

Another effective tuning of the Berry phase in a 3D TIs is the magnetic ion doping. Upon doping, the spin texture of topological surface state changes to a hedgehog-like spin texture, e.g., in a magnetic ion doped Bi₂Se₃, the surface state was gapped due to the ferromagnetic ordering, and the spin texture was turned to hedgehog like [36]. The Berry phase in such a magnetic ion doped topological insulator is defined by the spin texture of the Fermi surface, which, in this situation can be tuned from π to zero via shifting the Fermi level to the Dirac point [36,37]. The ferromagnetic state in a topological insulator is very useful, which enables the novel quantum anomalous Hall effect [38], and paves the way to dissipationless electronic conductance in zero magnetic field. Moreover, tuning the Berry phase to zero in a ferromagnetic TI also provides the condition for axion electrodynamics [36,39]. The ferromagnetic ordering

has been reported in 3d transition metal doped topological insulators, e.g., Mn:Bi₂Te₃ [40,41], Cr:TlBiTe₂ [42], and Cr:Bi₂Se₃ [43]. Recently, rare earth elements are also considered as magnetic dopants in TI materials, which provides ferromagnetism without significantly harming the high mobility [44,45]. Previous researches show that Gd is a good dopant in 3D TIs, for instance, Gd:Bi₂Te₃ shows antiferromagnetism [46], Gd:TlBiTe₂ and Gd:Bi₂Se₃ show ferromagnetism with large Gd moments (5-7 μ_B /Gd) [47,48]. Therefore, studying the magnetotransport properties of Gd doped topological insulators are helpful to understand the Berry phase. Here, we introduce a comprehensive magnetotransport study of Gd:Bi₂Se₃ single crystals to illustrate the nontrivial Berry phase in Gd doped TIs.

II. Experiments

A modified Bridgeman method was employed to grow the topological insulator single crystals (Bi₂Se₃ and Gd:Bi₂Se₃). Briefly, high-purity Gd (99.9%), Bi (99.99%), and Se (99.99%) powders (~10 g) in the stoichiometric ratio were mixed and sealed in a quartz tube as starting materials. For the Gd doped sample, the starting nominal ratio is Gd_{0.1}Bi_{1.9}Se₃. The crystal growth was carried out using the following procedure: i) Heating the mixed powders to 1100 °C in 1 °C/min to completely melt them; ii) Maintaining at this temperature for 24 h to ensure uniform mixture of Gd, Bi, and Se atoms; and iii) Slowly cooling down to 500 °C at 2 °C/h to crystallize the sample; iv) naturally cooling to room temperature. Since the Gd dopants possess a high melting point, we set the melting temperature at 1100 °C in step i) and ii) to ensure full interaction among the molten elements in the liquid state. After the growth process, single-crystal flakes with a typical size of 5 × 5 × 0.2 mm³ can be mechanically exfoliated from the ingot. The single crystals prefer to naturally cleave along the (001) planes, resulting in *c*-axis

being the normal direction of the flakes as is commonly the case in this family of materials. The dopant distribution of Gd:Bi₂Se₃ flakes was confirmed using X-ray energy dispersive spectroscopy (EDS) coupled to a scanning electron microscopy (SEM). In the present work, we employ the EDS results as the final composition, which is determined to be Gd_{0.02}Bi_{1.98}Se₃.

The electronic transport properties were measured using a physical properties measurement system (PPMS, Dynacool-14T, Quantum Design). Hall measurements were performed on a freshly cleaved *ab* plane, using room-temperature cured silver paste. The electric current was parallel to the *ab* plane while the magnetic field was perpendicular to the *ab* plane. The angle dependence of the magnetoresistance (MR) was measured using a horizontal rotational rig mounted on the PPMS. Before rotation, the sample alignment was designed to make sure that the magnetic field was always perpendicular to the electric current. The magnetic measurements were conducted using the vibration sample magnetometer (VSM) equipped on PPMS. During temperature dependent magnetization (MT) measurements, the samples were cooled to 3 K with 500 Oe magnetic field (FC mode) and zero magnetic field (ZFC mode), respectively, after which the magnetization data were collected in the heating process, with applied magnetic field of 500 Oe. Magnetic hysteresis (MH) curves were obtained by scanning the magnetic field between 5 T and -5 T at certain temperatures.

III. Results and Discussion

Before we conduct electronic transport measurements, EDS measurements were performed on freshly cleaved surface of crystals to analyze the distribution of Gd dopants. A relatively large area (500×670 μm²) was selected to conduct the measurements to ensure the accuracy of element ratio in the crystal, as shown in Fig. 1(a). The elemental mapping was superimposed to

SEM images to illustrate the elemental distribution with surface morphology. There're several wrinkles on the flat surface of the crystal, as demonstrated by the SEM image, which, however are not observed in elemental mapping image. The wrinkles are quite common on a cleaved quasi-two-dimensional crystal's surfaces. The SEM backscattered image and elemental mapping results suggest that the Gd dopant is uniformly distributed in the Bi_2Se_3 crystal without segregation. Further, we employ EDS to estimate the Gd doping level in the as-grown single crystals. Fig. 1(b) shows the characteristic peaks of all elements, in which the peak intensity related to the Bi and Se elements are much stronger than that of Gd element. After analyzing the peak intensity via the AZtec software, the elemental concentrations of two different Gd: Bi_2Se_3 samples are summarized in Table 1. The selenium vacancies are observed in both samples, which agrees with the literatures [33,49], and is the main reason for the Fermi level shifting into the conduction band. Gd doping level in both samples are stable at Gd/Bi ratio ~ 0.01 , which is much lower than the starting Gd/Bi ratio. Since the samples for EDS measurements are typical shiny single-crystal piece exfoliated from the ingot, we deduce that 1 atom% is a relatively stable doping level for Gd substitution at Bi sites in the aforementioned crystal growth process.

Before conducting electronic transport measurements on Gd: Bi_2Se_3 single crystals, we first revisit the electronic properties of Bi_2Se_3 single crystals grown with the same condition as that for Gd: Bi_2Se_3 crystals. The Bi_2Se_3 crystals possess a metallic ground state due to the Se vacancies. MR ($MR = [R(B) - R(0)]/R(0)$) in the 3–300 K and 0–14 T region are shown in Fig. 2(a). The total MR at low temperatures, e.g., below 30 K, are $\sim 20\%$ at 14 T, which slightly decrease to $\sim 10\%$ with heating. The observed roughly linear dependence of MR with the

magnetic field is also reported in other 3D TIs [30,50]. Another interesting point is that the low temperature MR vs. magnetic field curves show obvious oscillation behaviors at high fields, which is due to the Landau quantization, namely, the Shubnikov-de Haas (SdH) oscillation. The pure oscillation patterns for $3 \text{ K} \leq T \leq 30 \text{ K}$ can be obtained by subtracting the smooth MR backgrounds and are plotted against $1/B$ in Fig. 1(c). Note that, the background-subtracted oscillation patterns at different temperatures show exactly the same phases, however, with decreasing oscillation amplitude upon heating from 3 to 30 K. Therefore, the temperature-dependent SdH oscillation patterns are plotted in superposition [lower panel of Fig. 3(c)]. Since the Bi_2Se_3 crystals show metallic ground state, the SdH oscillations can be described by the Lifshitz-Kosevich (LK) formula, with the Berry phase being taken into account:

$$\frac{\Delta\rho}{\rho(0)} = \frac{5}{2} \left(\frac{B}{2F}\right)^{\frac{1}{2}} R_T R_D R_S \cos\left(2\pi\left(\frac{F}{B} + \gamma - \delta\right)\right)$$

Where $R_T = \alpha T \nu / B \sinh(\alpha T \mu / B)$, $R_D = \exp(-\alpha T_D \nu / B)$, and $R_S = \cos(\alpha g \nu / 2)$. Here, $\nu = m^*/m_0$ is the ratio of the effective cyclotron mass m^* to the free electron mass m_0 ; g is the g-factor; T_D is the Dingle temperature; and $\alpha = (2\pi^2 k_B m_0) / \hbar e$, where k_B is Boltzmann constant, \hbar is the reduced Planck constant, and e is the elementary charge. The oscillation of $\Delta\rho$ is described by the cosine term with a phase factor $\gamma - \delta$, in which $\delta = 0$ for 2D Fermi pockets, and $\pm 1/8$ for 3D Fermi pockets, $\gamma = 1/2 - \Phi_B/2$, where Φ_B is the Berry phase. The Berry phase of SdH oscillations can also be obtained by extrapolating the Landau level index n to the extreme field limit ($1/B \rightarrow 0$) in the Landau fan diagram, as shown in Fig. 2(d). Our resistivity measurements show that $\rho_{xx} \ll \rho_{xy}$ for Bi_2Se_3 crystals, we assign the maximum of the oscillations as half integer Landau indexes, the minimum of the oscillations as integer Landau indexes, respectively, and carefully fitted the data in straight lines [51,52]. As shown in Fig. 2(d),

the intercept of the straight line with the y-axis is zero, meaning that the Fermi pocket contributing to SdH oscillations in our Bi₂Se₃ single crystals are topologically trivial bulk bands. Further, angular dependence of SdH oscillation measurements is conducted to analyze the morphology of the related Fermi pocket, as shown in Fig. 2(b). The angular dependent SdH oscillation measurements are plotted in Fig. 2(c), the FFT results of which are shown in Fig. 2(e). The angular dependent SdH oscillations show 2D-like behavior, which is probably contributed by some 2D-like trivial bands. **Therefore, we deduce that the Fermi level is sitting on the edge of bulk conduction band, where the near-edge two-dimensional electron gas contributes mainly to the quantum oscillations [53-56].** The rest of the information obtained from the Bi₂Se₃ crystals together with the SdH of Gd:Bi₂Se₃ crystals will be discussed later.

Similarly, a freshly cleaved Gd:Bi₂Se₃ single crystal is employed to conduct MR measurements at various fixed temperatures, with applied external magnetic fields up to 14 T, as shown in Fig. 3(a). The quasi-linear MR with the magnetic field is similar to the observation in pure Bi₂Se₃ crystals, and the maximum MR values (e.g., MR at 14 T is ~ 8% below 50 K) decrease slightly with heating from 3 K. Another similarity is the low temperature oscillation patterns, which can be obtained by subtracting smooth backgrounds, as shown in Fig. 3(b). The SdH oscillation patterns are in phase with each other at different temperatures, however, the oscillation amplitudes decrease with heating, as described by the thermal damping factor in the LK formula. Let's pay attention to the Berry phase in Gd:Bi₂Se₃, obtained from the Landau fan diagram shown in Fig. 3(c). During linear fitting, we employ the same assigning rule as that for the Bi₂Se₃ crystals since $\rho_{xx} \ll \rho_{xy}$ also manifests here. The intercept of the straight line with the y-axis is 0.4, as shown in the zoom-in plot at high field limit [Inset of Fig. 3(c)]. Therefore,

a non-zero Berry phase of 0.8π was obtained with 1 atom% Gd doping in the Bi_2Se_3 . To further illustrate this point, we employ the LK formula to fit the oscillation patterns at 3 K, as shown in the inset of Fig. 3(b). A Berry phase of 0.78π was obtained from the fitting, which agrees well with that obtained from the Landau fan diagram. Further, we conducted magnetic measurements on the Gd: Bi_2Se_3 crystal to search for possible magnetic ordering which may contribute to the Berry phase. As shown in Fig. 3(d), the ZFC and FC curves coincide with each other perfectly and there's no obvious magnetic transition. The magnetism of trivalent lanthanide group ions originates from unpaired electrons, which can be described by the Curie law $\chi = C/T$ and Curie-Weiss law $\chi = C/(T + \theta_p)$. Here C is the Curie constant, and the Weiss constant θ_p typically accounts for the magnetic ordering of the electronic moments below the Curie or Neel temperature for uncorrelated spins. The fitting of the Curie-Weiss law is shown in the inset of Fig. 3(d), the obtained Curie constant C is ~ 2.5 emu K/mol and θ_p is ~ 0.4 K, which are neglectable. Here, $C = (N_A \mu_{\text{eff}}^2) / 3k_B$, where N_A is the Avogadro number, k_B is the Boltzmann constant, therefore, the effective momentum μ_{eff} of Gd is $\sim 4.5 \mu_B$. The MH curves at 3, 30, and 300 K also show paramagnetic behaviors, as shown in Fig. 3(f). Therefore, the Gd dopants in the crystals show paramagnetism, indicating that the origin of this Berry phase is not long-range magnetic ordering.

Further, one may learn the fermiology from the SdH oscillations using the LK formula, e.g., the area of Fermi pockets, the Fermi vector, Fermi velocity, and the cyclotron mass of electron, etc. According to the Onsager-Lifshitz equation, the frequency of quantum oscillations, $F = (\varphi_0 / 2\pi^2) A_F$, where A_F is the extremal cross-sectional area of the Fermi surface perpendicular to the magnetic field, and φ_0 is the magnetic flux quantum. The quantum

oscillation frequencies of Bi_2Se_3 and $\text{Gd}:\text{Bi}_2\text{Se}_3$ from the fast Fourier transform results in Fig. 2(f) and 3(e), are 157 T and 151 T, respectively. Therefore, the cross-section area A_F related to the Fermi pockets in Bi_2Se_3 and $\text{Gd}:\text{Bi}_2\text{Se}_3$ are 0.15 and 0.144 \AA^{-2} , respectively. Using $A_F = \pi k_F^2$, the Fermi wave vector k_F are 0.22 and 0.21 \AA^{-1} for the Bi_2Se_3 and $\text{Gd}:\text{Bi}_2\text{Se}_3$, respectively. According to the LK formula, the effective mass of carriers contributing to the SdH effect can be obtained through fitting the temperature dependence of the oscillation amplitude to the thermal damping factor R_T , which is shown in Fig. 4(a). During the fitting, we employ the normalized FFT amplitudes at various temperatures. The effective mass obtained from R_T fitting are $0.2m_e$ for Bi_2Se_3 and $0.16m_e$ for $\text{Gd}:\text{Bi}_2\text{Se}_3$. Thus, one can obtain the Fermi velocity $v_F = \hbar k_F / m^* \sim 2.2 \times 10^5$ m/s for Bi_2Se_3 and 2.8×10^5 m/s for $\text{Gd}:\text{Bi}_2\text{Se}_3$. From the field damping relationship, we fit the Dingle temperatures via Dingle plot, as shown in Fig. 4(b), for both samples, which are 32 and 21 K for Bi_2Se_3 and $\text{Gd}:\text{Bi}_2\text{Se}_3$, respectively. The quantum relaxation time and quantum mobility can also be obtained by $\tau = \hbar / 2\pi k_B T_D$ (3.8 and 5.8 fs for Bi_2Se_3 and $\text{Gd}:\text{Bi}_2\text{Se}_3$) and $\mu_Q = e\tau / m^*$ (310 and 637 cm^2/Vs for Bi_2Se_3 and $\text{Gd}:\text{Bi}_2\text{Se}_3$), respectively. The carrier's parameters calculated from the quantum oscillations are summarized in Table 2, together with carrier's density and mobility. The Hall measurements are also conducted on the Bi_2Se_3 and $\text{Gd}:\text{Bi}_2\text{Se}_3$ single crystals from 3 to 300 K, and the carrier's properties calculated from which are plotted in Fig. 4(c). Further, we conduct the angular dependent SdH measurements on a $\text{Gd}:\text{Bi}_2\text{Se}_3$ single crystal at 3 K, as shown in Fig. 5(a). The quantum oscillation patterns are clear in low angle area, which is similar to those for Bi_2Se_3 [Fig. 2(c)]. The oscillation frequencies can be obtained via FFT spectra, as shown in Fig. 5(b). Interestingly, the frequency seems not shifting obviously during the rotation of the crystal, which is different

from the 2D-like behavior in Bi_2Se_3 . Therefore, we plot the FFT frequencies of Bi_2Se_3 and $\text{Gd}:\text{Bi}_2\text{Se}_3$ against the rotation angle in Fig. 5(c). Note that, for a 2D Fermi surface, the angular-dependent SdH frequency $F(\theta)$ increases in an inverse cosine rule: $F(\theta) = F(0)/\cos(\theta)$, indicated by the light blue area in Fig. 5(c). As expected, the Bi_2Se_3 follows 2D rotation rule during rotation. However, the SdH frequencies of $\text{Gd}:\text{Bi}_2\text{Se}_3$ are roughly a constant during rotation, which indicates that the related Fermi pocket is not contributed by 2DEG. Further, we employ Landau fan diagram to analyze the Berry phase shifting at different rotation angles, which are also shown in Fig. 5(c). The Berry phase for Bi_2Se_3 is always zero, since its oscillations are contributed by 2DEG. However, for the $\text{Gd}:\text{Bi}_2\text{Se}_3$, the Berry phase keeps changing during rotation, regardless of the nearly constant frequency. Therefore, the Gd doping has a limited influence on the morphology of the Fermi surface, however contributes to the band topology of dramatically.

IV. Conclusions

We employed a modified Bridgeman method to grow Gd-doped Bi_2Se_3 single-crystal topological insulators. The Gd dopant distributes uniformly in the crystals, in which the doping level is ~ 1 atom% in Bi sites, as verified by EDS. The magnetic measurements show that no long-range magnetic ordering forms in $\text{Gd}:\text{Bi}_2\text{Se}_3$ crystals above 3 K, ruling out the possible magnetic ordering induced Berry phase. Magnetotransport measurements on $\text{Gd}:\text{Bi}_2\text{Se}_3$ single crystals show that Gd-doping has minor effects on SdH oscillation frequency, Fermi surface area, Fermi wave vectors, and effective electron mass of Bi_2Se_3 crystals. However, Gd-doping reduces the Hall mobility and carrier density, and modify the Berry phase and the morphology and topology of the Fermi pocket of Bi_2Se_3 , namely, the major contribution of Fermi pocket

changes from 2D-like electron gas states with trivial topology and zero Berry Phase to topological surface states with nontrivial topology and 0.8π Berry phase. The engineering of Berry phase by Gd doping may provide more possibility on application of topological insulators in electronic/spintronic devices.

Acknowledgements

This work is supported by National Natural Science Foundation of China (Grant No. 11974155). WZ, AB, DC, XW, JK acknowledge the supporting from ARC Centre of Excellence in Future Low-Energy Electronics Technologies No. CE170100039.

References

- [1] M. V. Berry, Quantal phase factors accompanying adiabatic changes, *Proc. Math. Phys. Eng. Sci.* **392**, 45 (1984).
- [2] J. Zak, Berry's phase for energy bands in solids, *Phys. Rev. Lett.* **62**, 2747 (1989).
- [3] G. Mikitik, and Y. V. Sharlai, Manifestation of Berry's phase in metal physics, *Phys. Rev. Lett.* **82**, 2147 (1999).
- [4] D. Shoenberg, *Magnetic oscillations in metals*, Cambridge university press, (2009).
- [5] X. Yuan, C. Zhang, Y. Liu, A. Narayan, C. Song, S. Shen, X. Sui, J. Xu, H. Yu, Z. An, J. Zhao, S. Sanvito, H. Yan, and F. Xiu, Observation of quasi-two-dimensional Dirac fermions in ZrTe₅, *NPG Asia Mater.* **8**, e325 (2016).
- [6] J. B. He, Y. Fu, L. X. Zhao, H. Liang, D. Chen, Y. M. Leng, X. M. Wang, J. Li, S. Zhang, M. Q. Xue, C. H. Li, P. Zhang, Z. A. Ren, and G. F. Chen, Quasi-two-dimensional massless Dirac fermions in CaMnSb₂, *Phys. Rev. B* **95**, 045128 (2017).
- [7] L. P. He, X. C. Hong, J. K. Dong, J. Pan, Z. Zhang, J. Zhang, and S. Y. Li, Quantum transport evidence for the three-dimensional Dirac semimetal phase in Cd₃As₂, *Phys. Rev. Lett.* **113**, 246402 (2014).
- [8] A. Narayanan, M. D. Watson, S. F. Blake, N. Bruyant, L. Drigo, Y. L. Chen, D. Prabhakaran, B. Yan, C. Felser, T. Kong, P. C. Canfield, and A. I. Coldea, Linear magnetoresistance caused by mobility fluctuations in n-doped Cd₃As₂, *Phys. Rev. Lett.* **114**, 117201 (2015).
- [9] X. Huang, L. Zhao, Y. Long, P. Wang, D. Chen, Z. Yang, H. Liang, M. Xue, H. Weng, Z. Fang, X. Dai, and G. Chen, Observation of the chiral-anomaly-induced negative magnetoresistance in 3D Weyl semimetal TaAs, *Phys. Rev. X* **5**, 031023 (2015).
- [10] J. Hu, J. Y. Liu, D. Graf, S. M. A. Radmanesh, D. J. Adams, A. Chuang, Y. Wang, I. Chiorescu, J. Wei, L. Spinu, and Z. Q. Mao, π Berry phase and Zeeman splitting of Weyl semimetal TaP, *Sci. Rep.* **6**, 18674 (2016).
- [11] P. Sergelius, J. Gooth, S. Baessler, R. Zierold, C. Wiegand, A. Niemann, H. Reith, C. Shekhar, C. Felser, B. Yan, and K. Nielsch, Berry phase and band structure analysis of the Weyl semimetal NbP, *Sci. Rep.* **6**, 33859 (2016).
- [12] M. Matusiak, J. R. Cooper, and D. Kaczorowski, Thermoelectric quantum oscillations in

- ZrSiS, *Nat. Commun.* **8**, 15219 (2017).
- [13] Q. Chen, Z. Lou, S. Zhang, B. Xu, Y. Zhou, H. Chen, S. Chen, J. Du, H. Wang, J. Yang, Q. Wu, O. V. Yazyev, and M. Fang, Large magnetoresistance and non-zero Berry phase in the nodal-line semimetal MoO₂, *Phys. Rev. B* **102**, 165133 (2020).
- [14] J. Liu, P. Liu, K. Gordon, E. Emmanouilidou, J. Xing, D. Graf, B. C. Chakoumakos, Y. Wu, H. Cao, D. Dessau, Q. Liu, and N. Ni, Nontrivial topology in the layered Dirac nodal-line semimetal candidate SrZnSb₂ with distorted Sb square nets, *Phys. Rev. B* **100**, 195123 (2019).
- [15] Y. Yang, H. Xing, G. Tang, C. Hua, C. Yao, X. Yan, Y. Lu, J. Hu, Z. Mao, and Y. Liu, Anisotropic Berry phase in the Dirac nodal-line semimetal ZrSiS: The effect of spin-orbit coupling, *Phys. Rev. B* **103**, 125160 (2021).
- [16] R. Singha, A. K. Pariari, B. Satpati, and P. Mandal, Large nonsaturating magnetoresistance and signature of nondegenerate Dirac nodes in ZrSiS, *Proc. Natl. Acad. Sci. U.S.A.* **114**, 2468 (2017).
- [17] S. Li, Z. Guo, D. Fu, X. C. Pan, J. Wang, K. Ran, S. Bao, Z. Ma, Z. Cai, R. Wang, R. Yu, J. Sun, F. Song, and J. Wen, Evidence for a Dirac nodal-line semimetal in SrAs₃, *Sci. Bull.* **63**, 535 (2018).
- [18] L. Guo, T. W. Chen, C. Chen, L. Chen, Y. Zhang, G. Y. Gao, J. Yang, X. G. Li, W. Y. Zhao, and S. Dong, Electronic transport evidence for topological nodal-line semimetals of ZrGeSe single crystals, *ACS Appl. Electron.* **1**, 869 (2019).
- [19] S. Xu, L. Zhou, H. Wang, X. Y. Wang, Y. Su, P. Cheng, H. Weng, and T. L. Xia, Quantum oscillations and electronic structure in the large-Chern number semimetal RhSn, *Phys. Rev. B* **100**, 245146 (2019).
- [20] L. Ye, M. K. Chan, R. D. McDonald, D. Graf, M. Kang, J. Liu, T. Suzuki, R. Comin, L. Fu, and J. G. Checkelsky, de Haas-van Alphen effect of correlated Dirac states in kagome metal Fe₃Sn₂, *Nat. Commun.* **10**, 4870 (2019).
- [21] Y. Fang, F. Tang, Y. R. Ruan, J. M. Zhang, H. Zhang, H. Gu, W. Y. Zhao, Z. D. Han, W. Tian, B. Qian, X. F. Jiang, X. M. Zhang, and X. Ke, Magnetic-field-induced nontrivial electronic state in the Kondo-lattice semimetal CeSb, *Phys. Rev. B* **101**, 094424 (2020).
- [22] K. A. M. H. Siddiquee, R. Munir, C. Dissanayake, X. Hu, S. Yadav, Y. Takano, E. S. Choi, D. Le, T. S. Rahman, and Y. Nakajima, Fermi surfaces of the topological semimetal CaSn₃ probed through de Haas van Alphen oscillations, *J. Phys. Condens. Matter* **33**, 17LT01 (2021).
- [23] I. A. Luk'yanchuk, and Y. Kopelevich, Phase analysis of quantum oscillations in graphite, *Phys. Rev. Lett.* **93**, 166402 (2004).
- [24] Y. B. Zhang, Y. W. Tan, H. L. Stormer, and P. Kim, Experimental observation of the quantum Hall effect and Berry's phase in graphene, *Nature* **438**, 201 (2005).
- [25] H. Murakawa, M. S. Bahramy, M. Tokunaga, Y. Kohama, C. Bell, Y. Kaneko, N. Nagaosa, H. Y. Hwang, and Y. Tokura, Detection of Berry's phase in a bulk rashba semiconductor, *Science* **342**, 1490 (2013).
- [26] O. Erten, P. Ghaemi, and P. Coleman, Kondo breakdown and quantum oscillations in SmB₆, *Phys. Rev. Lett.* **116**, 046403 (2016).
- [27] G. Li, Z. Xiang, F. Yu, T. Asaba, B. Lawson, P. Cai, C. Tinsman, A. Berkley, S. Wolgast, and Y. S. Eo, Two-dimensional Fermi surfaces in Kondo insulator SmB₆, *Science* **346**, 1208 (2014).
- [28] Z. Xiang, Y. Kasahara, T. Asaba, B. Lawson, C. Tinsman, L. Chen, K. Sugimoto, S.

- Kawaguchi, Y. Sato, and G. Li, Quantum oscillations of electrical resistivity in an insulator, *Science* **362**, 65 (2018).
- [29] N. Zhang, G. Zhao, L. Li, P. Wang, L. Xie, B. Cheng, H. Li, Z. Lin, C. Xi, and J. Ke, Magnetotransport signatures of Weyl physics and discrete scale invariance in the elemental semiconductor tellurium, *Proc. Natl. Acad. Sci. U.S.A.* **117**, 11337 (2020).
- [30] W. Zhao, L. Chen, Z. Yue, Z. Li, D. Cortie, M. Fuhrer, and X. Wang, Quantum oscillations of robust topological surface states up to 50 K in thick bulk-insulating topological insulator, *npj Quantum Mater.* **4**, 1 (2019).
- [31] H. Zhang, C. X. Liu, X. L. Qi, X. Dai, Z. Fang, and S. C. Zhang, Topological insulators in Bi_2Se_3 , Bi_2Te_3 and Sb_2Te_3 with a single Dirac cone on the surface, *Nat. phys.* **5**, 438 (2009).
- [32] Y. Chen, J. G. Analytis, J. H. Chu, Z. Liu, S. K. Mo, X. L. Qi, H. Zhang, D. Lu, X. Dai, and Z. Fang, Experimental realization of a three-dimensional topological insulator Bi_2Te_3 , *science* **325**, 178 (2009).
- [33] M. Busch, O. Chiatti, S. Pezzini, S. Wiedmann, J. Sánchez-Barriga, O. Rader, L. V. Yashina, and S. F. Fischer, High-temperature quantum oscillations of the Hall resistance in bulk Bi_2Se_3 , *Sci. Rep.* **8**, 1 (2018).
- [34] A. Taskin, and Y. Ando, Berry phase of nonideal Dirac fermions in topological insulators, *Phys. Rev. B* **84**, 035301 (2011).
- [35] Z. Ren, A. Taskin, S. Sasaki, K. Segawa, and Y. Ando, Large bulk resistivity and surface quantum oscillations in the topological insulator $\text{Bi}_2\text{Te}_2\text{Se}$, *Phys. Rev. B* **82**, 241306 (2010).
- [36] S. Y. Xu, M. Neupane, C. Liu, D. Zhang, A. Richardella, L. A. Wray, N. Alidoust, M. Leandersson, T. Balasubramanian, and J. Sánchez-Barriga, Hedgehog spin texture and Berry's phase tuning in a magnetic topological insulator, *Nat. Phys.* **8**, 616 (2012).
- [37] H. Z. Lu, J. Shi, and S. Q. Shen, Competition between weak localization and antilocalization in topological surface states, *Phys. Rev. Lett.* **107**, 076801 (2011).
- [38] C. Z. Chang, J. Zhang, X. Feng, J. Shen, Z. Zhang, M. Guo, K. Li, Y. Ou, P. Wei, and L. L. Wang, Experimental observation of the quantum anomalous Hall effect in a magnetic topological insulator, *Science*, **340**, 167 (2013).
- [39] A. M. Essin, J. E. Moore, and D. Vanderbilt, Magnetoelectric polarizability and axion electrodynamics in crystalline insulators, *Phys. Rev. Lett.* **102**, 146805 (2009).
- [40] Y. Hor, P. Roushan, H. Beidenkopf, J. Seo, D. Qu, J. Checkelsky, L. Wray, D. Hsieh, Y. Xia, and S. Y. Xu, Development of ferromagnetism in the doped topological insulator $\text{Bi}_{2-x}\text{Mn}_x\text{Te}_3$, *Phys. Rev. B* **81**, 195203 (2010).
- [41] J. G. Checkelsky, J. Ye, Y. Onose, Y. Iwasa, and Y. Tokura, Dirac-fermion-mediated ferromagnetism in a topological insulator, *Nat. Phys.* **8**, 729 (2012).
- [42] Z. Wang, K. Segawa, S. Sasaki, A. Taskin, and Y. Ando, Ferromagnetism in Cr-doped topological insulator TlSbTe_2 , *APL Mater.* **3**, 083302 (2015).
- [43] P. Haazen, J. B. Laloë, T. Nummy, H. Swagten, P. Jarillo-Herrero, D. Heiman, and J. Moodera, Ferromagnetism in thin-film Cr-doped topological insulator Bi_2Se_3 , *Appl. Phys. Lett.* **100**, 082404 (2012).
- [44] W. Zhao, C. X. Trang, Q. Li, L. Chen, Z. Yue, A. Bake, C. Tan, L. Wang, M. Nancarrow, and M. Edmonds, Massive Dirac fermions and strong Shubnikov–de Haas oscillations in single crystals of the topological insulator Bi_2Se_3 doped with Sm and Fe, *Phys. Rev. B* **104**, 085153 (2021).
- [45] T. Chen, W. Liu, F. Zheng, M. Gao, X. Pan, G. Van Der Laan, X. Wang, Q. Zhang, F. Song, and B. Wang, High-mobility Sm-doped Bi_2Se_3 ferromagnetic topological insulators and

- robust exchange coupling, *Adv. Mater.* **27**, 4823 (2015).
- [46] J. Kim, K. Lee, T. Takabatake, H. Kim, M. Kim, and M. H. Jung, Magnetic transition to antiferromagnetic phase in gadolinium substituted topological insulator Bi_2Te_3 , *Sci. Rep.* **5**, 1 (2015).
- [47] S. Filnov, I. I. Klimovskikh, D. Estyunin, A. Fedorov, V. Y. Voroshnin, A. Koroleva, A. G. Rybkin, E. Shevchenko, Z. S. Aliev, and M. Babanly, Probe-dependent Dirac-point gap in the gadolinium-doped thallium-based topological insulator $\text{TlBi}_{0.9}\text{Gd}_{0.1}\text{Se}_2$, *Phys. Rev. B* **102**, 085149 (2020).
- [48] Y. Song, F. Yang, M. Y. Yao, F. Zhu, L. Miao, J. P. Xu, M. X. Wang, H. Li, X. Yao, and F. Ji, Large magnetic moment of gadolinium substituted topological insulator: $\text{Bi}_{1.98}\text{Gd}_{0.02}\text{Se}_3$, *Appl. Phys. Lett.* **100**, 242403 (2012).
- [49] A. Tayal, D. Kumar, and A. Lakhani, Role of lattice inhomogeneities on the electronic properties of selenium deficient Bi_2Se_3 , *J. Phys. Condens. Matter.* **29**, 445704 (2017).
- [50] M. Novak, S. Sasaki, K. Segawa, and Y. Ando, Large linear magnetoresistance in the Dirac semimetal TlBiSSe , *Phys. Rev. B* **91**, 041203 (2015).
- [51] W. Zhao, D. Cortie, L. Chen, Z. Li, Z. Yue, and X. Wang, Quantum oscillations in iron-doped single crystals of the topological insulator Sb_2Te_3 , *Phys. Rev. B* **99**, 165133 (2019).
- [52] F. X. Xiang, X. L. Wang, M. Veldhorst, S. X. Dou, and M.S. Fuhrer, Observation of topological transition of Fermi surface from a spindle torus to a torus in bulk Rashba split BiTeCl , *Phys. Rev. B* **92**, 035123 (2015).
- [53] P. King, R. C. Hatch, M. Bianchi, R. Ovsyannikov, C. Lupulescu, G. Landolt, B. Slomski, J. Dil, D. Guan, and J. Mi, Large tunable Rashba spin splitting of a two-dimensional electron gas in Bi_2Se_3 , *Phys. Rev. Lett.* **107**, 096802 (2011).
- [54] M. Bianchi, R. C. Hatch, J. Mi, B. B. Iversen, and P. Hofmann, Simultaneous quantization of bulk conduction and valence states through adsorption of nonmagnetic impurities on Bi_2Se_3 , *Phys. Rev. Lett.* **107**, 086802 (2011).
- [55] H. M. Benia, C. Lin, K. Kern, and C. R. Ast, Reactive chemical doping of the Bi_2Se_3 topological insulator, *Phys. Rev. Lett.* **107**, 177602 (2011).
- [56] M. Bianchi, D. Guan, S. Bao, J. Mi, B. B. Iversen, P. D. King, and P. Hofmann, Coexistence of the topological state and a two-dimensional electron gas on the surface of Bi_2Se_3 , *Nat. comm.* **1**, 1 (2010).

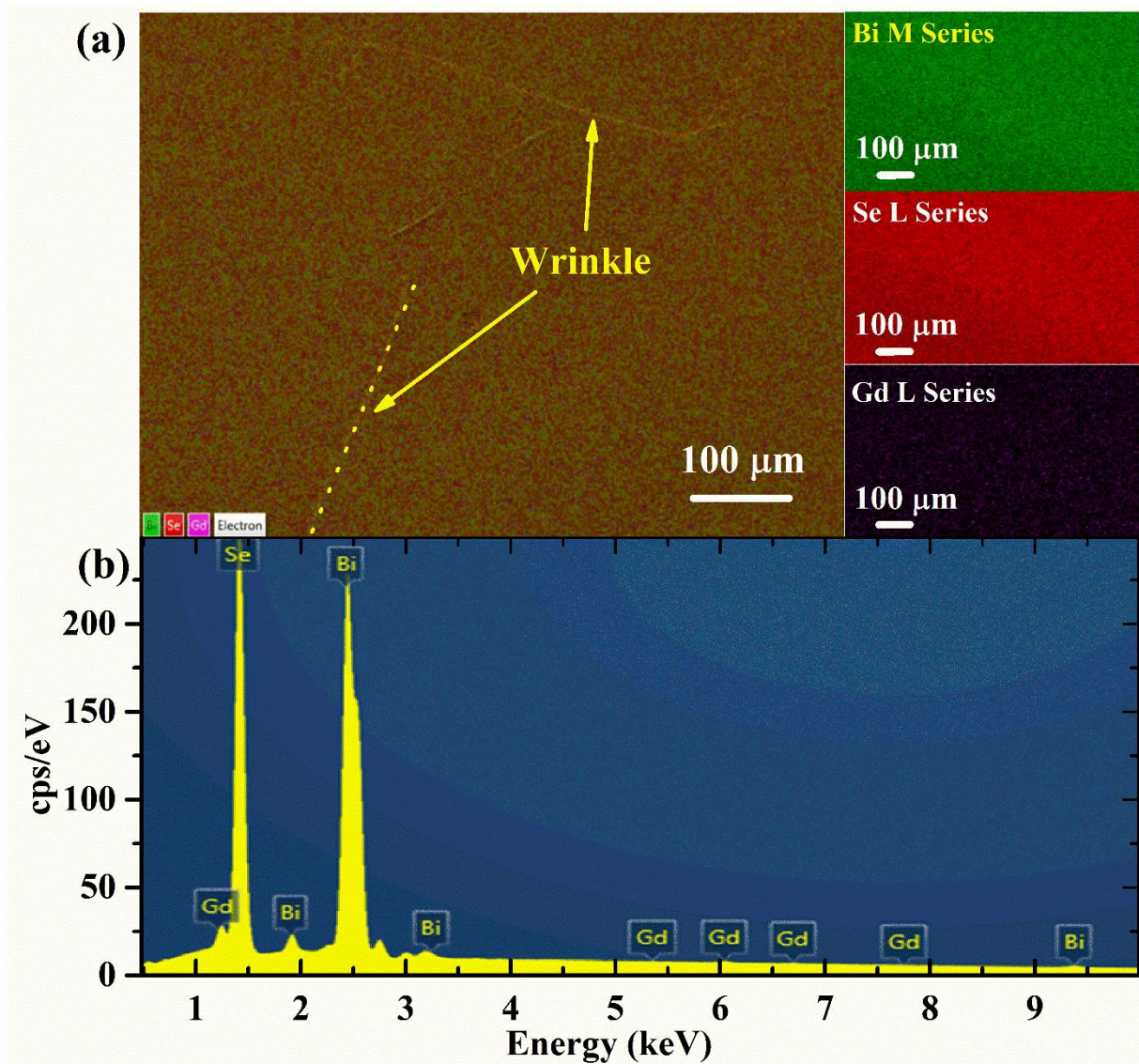


Fig. 1. SEM and EDS characterization of a freshly cleaved Gd:Bi₂Se₃ single-crystal surface. (a) The secondary electron image and elemental mapping image are plotted in superposition to illustrate the uniform distribution of all elements. The element mapping of Bi, Se and Gd in the same area are shown separately on the right side. (b) The energy dispersive spectroscopy of the

area scan, in which the peaks are indexed with elements.

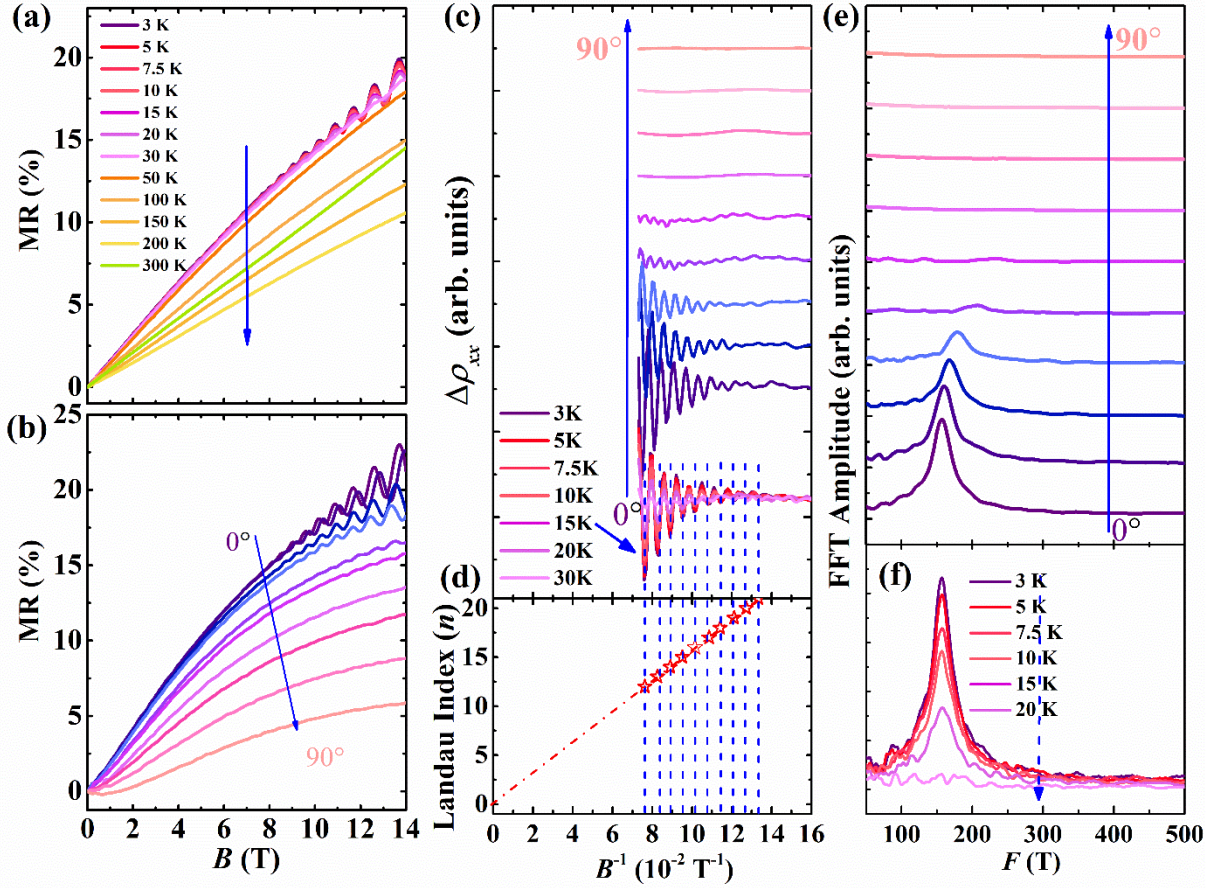


Fig. 2. A glimpse of the magnetotransport properties of a pure Bi₂Se₃ single crystal. (a, b) Temperature and angle ($T=3$ K) dependence of the MR vs. B curves. (c) Temperature and angle dependent oscillation patterns whose amplitude decreases with heating (plotted in superposition of all temperatures, as pointed by the blue arrow) and increasing rotating angle. (d) The Landau fan diagram of the oscillation patterns at 0 degree. (e, f) FFT amplitude plot during rotating and heating.

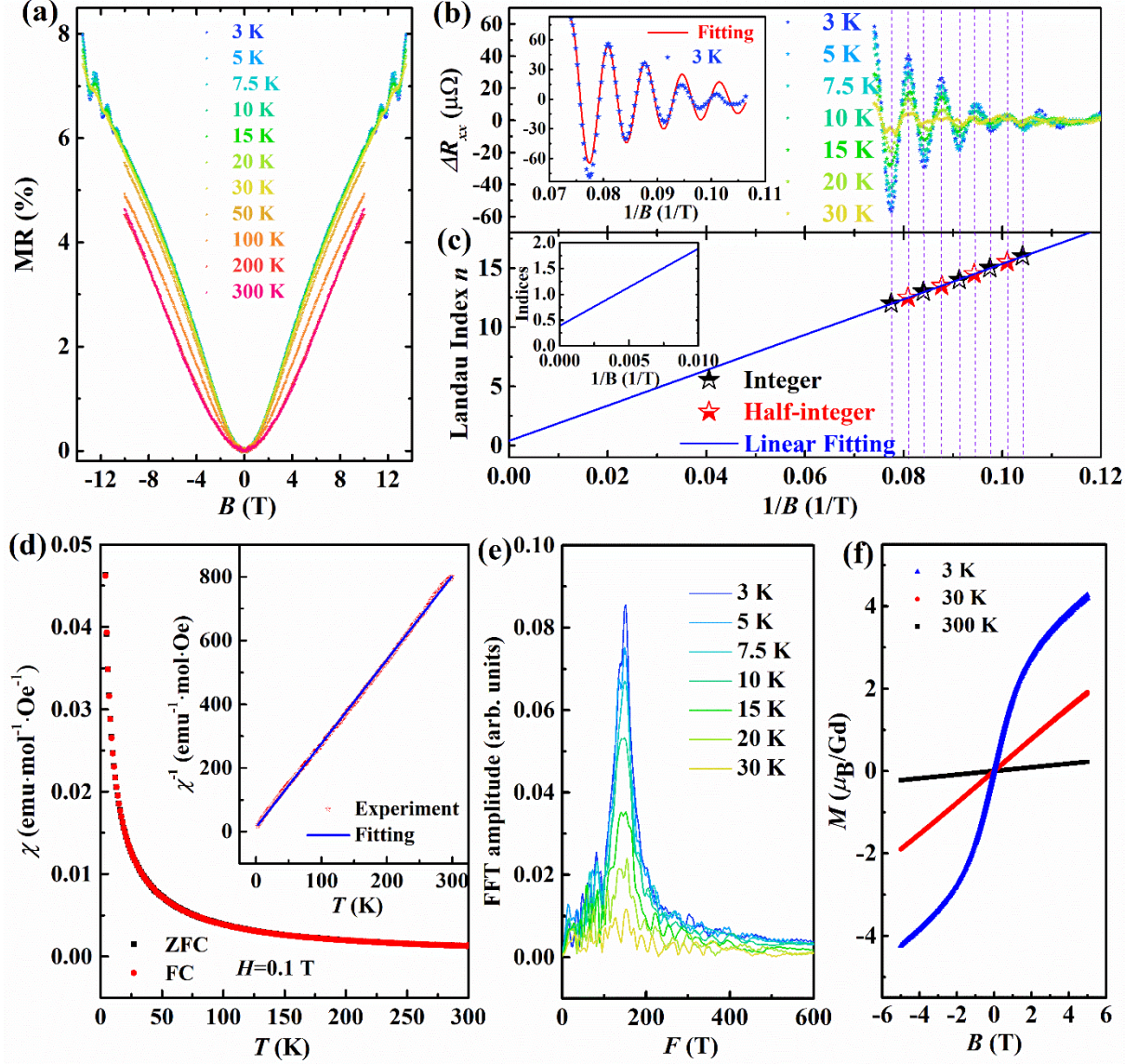


Fig. 3. A glimpse of the magnetotransport and magnetic properties of a Gd:Bi₂Se₃ single crystal. (a) MR vs. B curves at fixed temperatures ranging from 3 to 300 K. (b) The oscillatory patterns of the MR vs. $1/B$ curves. Inset: A fitting of the 3-K oscillatory pattern using the LK formula. (c) The Landau fan diagram is plotted to illustrate the Berry phase, in which the dot lines are guiding between the oscillation peaks and dips. (d) Temperature dependence of the ZFC and FC magnetic susceptibility. Inset: a fitting of the magnetic data using the Curie-Weiss law. (e) The FFT spectra of oscillatory patterns. (f) Magnetic hysteresis loops at $T=3, 30,$ and 300 K.

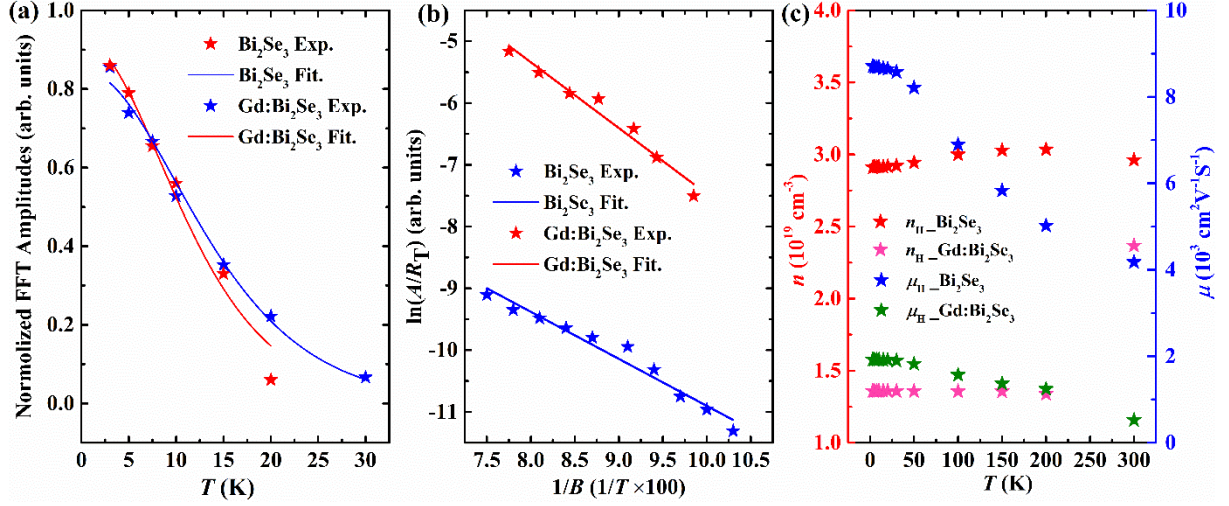


Fig. 4. The carrier's properties of Bi_2Se_3 and $\text{Gd}:\text{Bi}_2\text{Se}_3$ single crystals. (a) The LK formula fitting to obtain the effective mass of electrons. (b) The Dingle plots. (c) Temperature dependence of the carrier density and mobility obtained from Hall measurements.

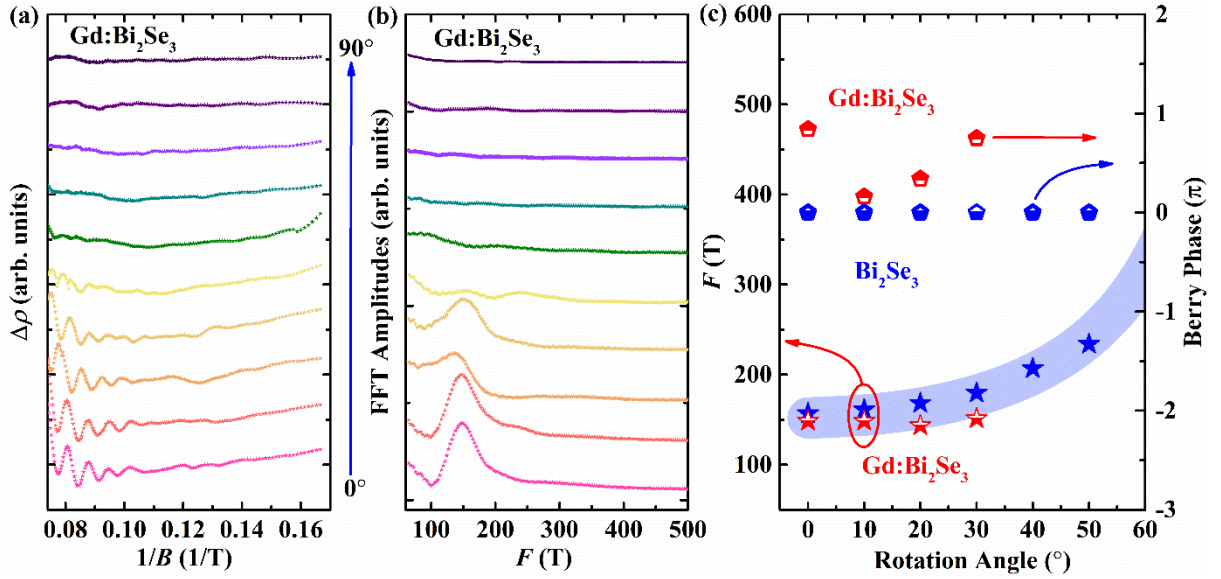


Fig. 5. Angular dependent SdH oscillations of $\text{Gd}:\text{Bi}_2\text{Se}_3$ single crystals. (a) The SdH oscillation patterns obtained from the angular dependent MR curves from which smooth backgrounds have been subtracted. (b) FFT spectra of the oscillation patterns in Panel (a). (c) The SdH oscillation frequencies and Berry phase are plotted as a function of the rotation angle. Note that, the light blue area indicates the frequency change of an ideal 2D Fermi surface.

Table 1. Elemental concentration of Gd:Bi₂Se₃ single crystals.

Bi ₂ Se ₃ crystals	Bi (atom%)	Se (atom%)	Gd (atom%)
Sample 1	40	59.6	0.4
Sample 2	40.3	59.2	0.4

Table 2. The quantum oscillation and carrier's parameters at $T=3$ K: SdH frequency F , cross-sectional Fermi surface area A_F , Fermi vector k_F , effective electron mass m^* , Fermi velocity v_F , quantum mobility μ_Q , carrier density (n_{H_3K}) and mobility (μ_{H_3K}) from Hall measurements, and the Berry phase Φ_B .

	F (T)	A_F (\AA^{-2})	k_F (\AA^{-1})	m^* (m_e)	v_F (m/s)	μ_Q (cm^2/Vs)	n_{H_3K} (cm^{-3})	μ_{H_3K} (cm^2/Vs)	Φ_B
Bi ₂ Se ₃	157	0.15	0.22	0.2	2.2×10^5	310	2.8×10^{19}	8400	0
Gd:Bi ₂ Se ₃	151	0.14	0.21	0.16	2.8×10^5	637	1.38×10^{19}	1500	0.8π